Title

Histone deposition pathways determine the chromatin landscapes of H3.1 and H3.3 K27M oncohistones

Authors

Jay F. Sarthy[1,2], Michael P. Meers[1], Derek H. Janssens[1], Jorja G. Henikoff[1], Heather Feldman[4], Patrick J. Paddison[4], Christina M. Lockwood[5], Nicholas A. Vitanza[2,3], James M. Olson[2,3], Kami Ahmad[1]*, and Steven Henikoff[1,6]*

[1]Basic Sciences Division, Fred Hutchinson Cancer Research Center, 1100 N. Fairview Ave, Seattle, WA, 98109

[2]Cancer and Blood Disorders, 4800 Sand Point Way, Seattle Children's Hospital, Seattle, WA, 98105

[3]Clinical Research Division Fred Hutchinson Cancer Research Center, 1100 N. Fairview Ave, Seattle, WA, 98109

[4]Human Biology Division, Fred Hutchinson Cancer Research Center, 1100 N. Fariview Ave, Seattle, WA, 98109

[5]Department of Laboratory Medicine and Pathology, University of Washington School of Medicine, Seattle, WA, 98195.

[6]Howard Hughes Medical Institute

*corresponding authors: kahmad@fredhutch.org steveh@fhcrc.org

Short title

Profiling Chromatin Landscapes in DMGs

Abstract

Lysine 27-to-methionine (K27M) mutations in the H3.1 or H3.3 histone genes are characteristic of pediatric diffuse midline gliomas (DMGs). These oncohistone mutations dominantly inhibit histone H3K27 trimethylation and silencing, but it is unknown how oncohistone type affects gliomagenesis. We show that the genomic distributions of H3.1 and H3.3 oncohistones in human patient-derived DMG cells are consistent with the DNA replication-coupled deposition of histone H3.1 and the predominant replication-independent deposition of histone H3.3. Although H3K27 trimethylation is reduced for both oncohistone types, H3.3K27M-bearing cells retain some domains, and only H3.1K27M-bearing cells lack H3K27 trimethylation. Neither oncohistone interferes with PRC2 binding. Using Drosophila as a model, we demonstrate that inhibition of H3K27 trimethylation occurs only when H3K27M oncohistones are deposited into chromatin and only when expressed in cycling cells. We propose that oncohistones inhibit the H3K27 methyltransferase as chromatin patterns are being duplicated in proliferating cells, predisposing them to tumorigenesis.

Introduction

Diffuse midline gliomas (DMGs) are lethal pediatric brain tumors associated with mutations in genes encoding either histone H3.1 or H3.3, most frequently the lysine 27-to-methionine (H3K27M) "oncohistone" substitutions (Schwartzentruber *et al*, 2012; Wu *et al*, 2012). H3K27M oncohistones cause the global reduction of histone H3 lysine 27 trimethylation (H3K27me3), a covalent modification that marks silenced regions in the genome. Since H3K27M oncohistones comprise only ~5-15% of the total H3 histone within DMG cells (Chan *et al*, 2013; Lewis *et al*, 2013), they are thought to dominantly inhibit the H3K27 methyltransferase Enhancer of Zeste Homologue-2 (EZH2). Indeed, an H3K27M peptide binds in the active site of EZH2 and inhibits catalytic activity *in vitro*, and ectopic expression of either oncohistone inhibits H3K27 methylation *in vivo* (Chan *et al*, 2013; Lewis *et al*, 2013; Bender *et al*, 2013; Justin *et al*, 2016; Stafford *et al*, 2018). These studies have led to the hypothesis that oncohistones inhibit Polycomb-mediated repression of oncogenes, predisposing cells to tumorigenesis.

Most DMG patients carry K27M mutations in the genes encoding the histone variant H3.3, and only ~20% of mutations are in histone H3.1 genes (Wu et al, 2012; Fontebasso et al, 2014). This ratio is surprising given that there are only two genes encoding H3.3 and 12 genes encoding H3.1 in the human genome. In addition, although these two histones are very similar, H3.3 or H3.1 K27M mutations are associated with distinct sets of secondary mutations in cancers, and H3.1 mutations are associated with earlier onset gliomagenesis. Finally, while the H3.3 mutations are restricted to gliomas, H3.1 mutations have also been identified in AML and melanomas (Mackay et al, 2017; Nacev et al, 2019; Lehnertz et al, 2017). These differences suggest that the two oncohistones differ in tumorigenic effects.

Studies in mammalian cells suggest that both H3.1K27M and H3.3K27M oncohistones require cell cycle progression in order to inhibit EZH2 (Chan et al, 2013; Nagaraja et al, 2019), though the etiology of this dependency remains unknown. Histone H3.1 is massively produced only in S phase of the cell cycle, but histone H3.3 is produced constitutively. While the bulk of histone deposition occurs during DNA replication as new chromatin is assembled, the H3.3 histone is deposited both during DNA replication and at sites of active histone turnover, and these are evolutionarily conserved properties of the two histone types (Ahmad &Henikoff, 2002; Tagami et al, 2004; Drane et al, 2010; Ray-Gallet et al, 2011; Clement et al, 2018). Capitalizing on this conservation, we use Drosophila to show that overexpressing either H3K27M oncohistone inhibits H3K27 methylation only in cells progressing through S-phase and only if deposited into chromatin. To directly assess the genomic distribution of H3.3 and H3.1 K27M oncohistones, we applied CUT&RUN chromatin profiling (Skene & Henikoff, 2017) to a panel of patient-derived DMG cell lines. We demonstrate that the H3.1 K27M oncohistone is distributed across the genome, consistent with replication-coupled deposition, and these cells have very low H3K27 methylation throughout the genome. In contrast, the bulk of H3.3 K27M oncohistone localizes to sites of active histone turnover, although we also detect the oncohistone at a low level genome-wide, which is consistent with H3.3 deposition during DNA replication. While H3.3K27M-bearing cells have low global levels of H3K27 methylation, they retain high level methylation at a small number of domains. Finally, we find that neither H3K27M oncohistone interferes with PRC2 binding to chromatin in DMG cells. These results support a model where H3K27M oncohistones inhibit PRC2 on chromosomes, and have implications for the origin of gliomas during proliferative periods in development and explain the spectra of secondary mutations in these gliomas.

Results

Chromatin-bound K27M histone inhibits H3K27 trimethylation in cycling cells

Histone H3 variants are highly conserved across evolution, and identical H3.3 histones are produced in both humans and Drosophila (Ahmad & Henikoff, 2002). Humans have two replication-dependent H3-type histones – H3.1 and H3.2 – while Drosophila has only one, which is identical to H3.2. Therefore, to dissect the inhibition of H3K27 methylation by oncohistone variant types, we used Drosophila cell and animal models. We first transfected Drosophila S2 cells to overexpress FLAG epitope-tagged wildtype or H3K27M oncohistone constructs, and allowed cells to progress through 2-3 cell cycles with expression of the transfected constructs. Nuclei that overexpress tagged histone H3.2 or H3.3 show broad staining for H3K27 trimethylation at similar levels as untransfected control nuclei (Figure 1A,B). In contrast, the same constructs with a K27M mutation show dramatic reduction of H3K27me3 (Figure 1A,B). These results show that both H3.2 and H3.3 K27M oncohistones can inhibit H3K27 methylation to similar degrees, at least when similarly overexpressed.

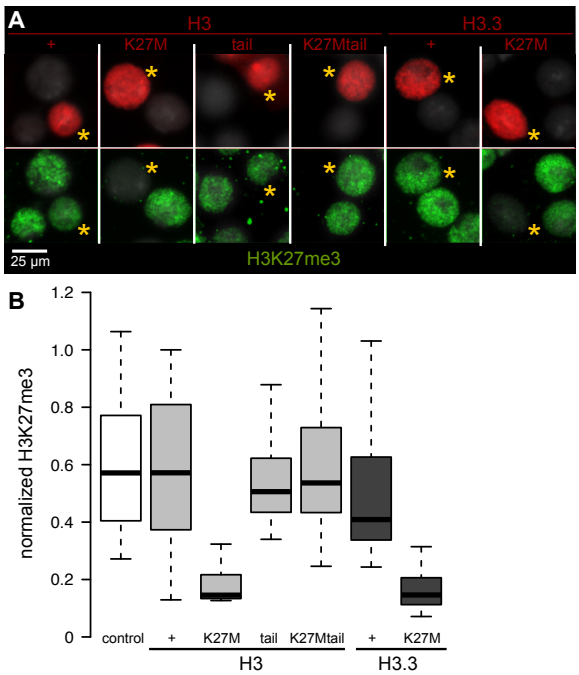

Figure 1. Chromatin-bound K27M histones inhibit H3K27 trimethylation. Drosophila S2 cells were transfected with epitope-tagged histone constructs, and immunostained for H3K27 trimethylation (green) after two days of protein (red) expression. (A) Representative images of non-transfected cells and cells transfected with the indicated epitope-tagged histone construct (yellow asterisks). (B) The mean signal intensity of 50 transfected nuclei and of 50 non-transfected nuclei from two transfections for each construct is plotted.

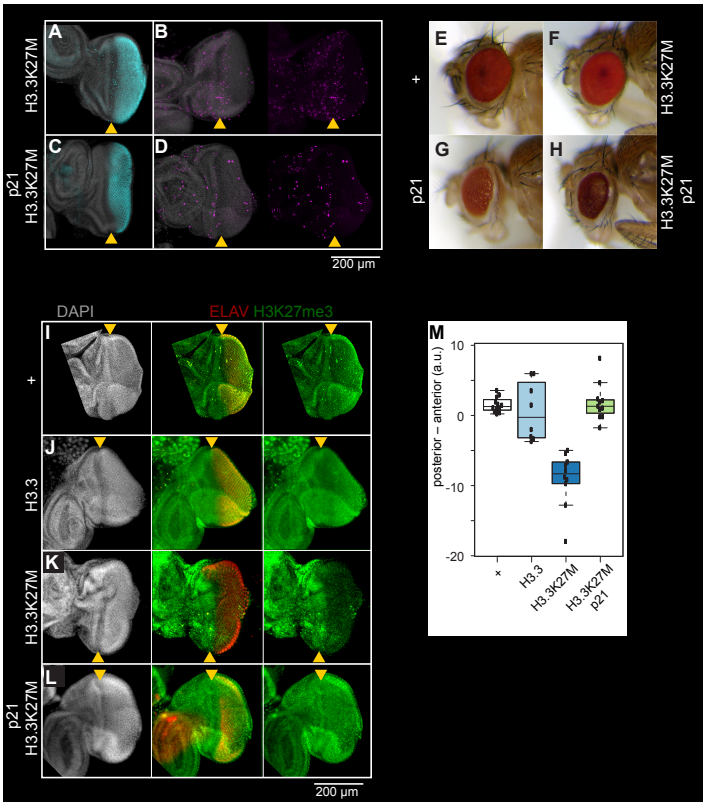

Figure 2. Inhibition of H3K27 methylation by K27M histones is limited to cycling cells. Eye imaginal discs from late larvae are divided by the morphogenetic furrow (MF, yellow arrowhead) into an anterior region (left) with asynchronously dividing cells and a posterior region (right). Discs were immunostained for the ELAV neuronal marker (red), which marks differentiating photoreceptors in the posterior region of the disc, the H3K27me3 modification (green), the H3.3K27M oncohistone (blue), or for mitotic cells (S10-phosphorylation, magenta). (A,B) In eye imaginal discs, one last wave of mitosis occurs in the posterior portion (to the right) of the disc behind the MF, as cells initiate neuronal differentiation. The *GMR-GAL4* driver induces expression of the H3.3K27M oncohistone in this region of the disc. (C,D) Expression of the S phase inhibitor p21 in the posterior region of the eye disc blocks progression of the last cell cycle, indicated by the absence of mitotic cells in the posterior region of the eye disc. *GMR-GAL4* induced expression of the H3.3K27M oncohistone in the posterior region of the disc is unaffected. (E,F) Adult eye morphology is unaffected by expression of either a wildtype H3.3 transgene or an H3.3K27M transgene late in development by the *GMR-GAL4* driver. (G,H) GMR-induced expression of the cell cycle inhibitor p21 results in moderately reduced eye size in both wildtype (G) and H3.3K27M-expressing animals (H). (I) Eye imaginal discs from wildtype larvae show high H3K27me3 signal apparent in both the anterior and posterior regions of the eye disc. (J) Induced overexpression of a wildtype H3.3 histone in the posterior portion of the eye disc does not affect H3K27me3 staining. (K) Induced overexpression of H3.3K27M histone strongly reduces H3K27me3 staining in the posterior region of the eye disc. (L) Co-expression of H3.3K27M and the p21 inhibitor show high level H3K27me3 staining in both the anterior and posterior regions of the eye disc. (M) Quantification of H3K27me3 signal intensity differences between the anterior portion of eye discs and the posterior portion, where the *GMR-GAL4* driver induces histone transgene expression. At least 10 discs were measured for each genotype.

A soluble H3K27M tail peptide can inhibit the EZH2 methyltransferase *in vitro* (Lewis et al, 2013), so we introduced a construct encoding only the histone H3.2 N-terminal tail (residues 1-44) fused to Red Fluorescent Protein (RFP). This H3 tail protein cannot incorporate into nucleosomes as it lacks a histone fold domain, but a large fraction of it localizes within the nucleus (Figure 1A). We observed that H3K27 trimethylation levels are unaffected in cells expressing either the wildtype histone tail or the K27M histone tail fusion protein (Figure 1A,B). Thus, we infer that while the H3K27M oncohistone can block H3K27 trimethylation, it must be incorporated into chromatin to do so.

Incorporation of H3.1 and H3.2 histones into chromatin is coupled to DNA replication as new nucleosomes are assembled behind replication forks (Ahmad & Henikoff, 2002; Tagami et al, 2004). Expression of a H3.3K27M mutant histone in developing wing imaginal discs inhibits H3K27 trimethylation and Polycomb-mediated silencing (Herz et al, 2014; Ahmad & Spens, 2019). To determine if the H3K27M oncohistone can inhibit methylation in both cycling and in non-dividing cells, we used the developing Drosophila eye as a system where we could control induction of histone proteins during the last developmentally-instructed cell division. Following proliferation of eye progenitor cells, one last synchronized wave of cell division moves across a disc just posterior to the morphogenetic furrow (MF) (Figure 2A). The late-eye-specific *GMR-GAL4* driver produces the GAL4 activator only in the posterior portion of the disc, and thus induction of a GAL4-responsive histone transgene will produce the protein only in cells that are destined to go through only one more division before terminally differentiating into photoreceptors (Figure 2A). Since we found that H3 and H3.3 oncohistones behave similarly when overexpressed in Drosophila cell culture, we used this GAL4 system to overexpress wildtype H3.3 or H3.3K27M histones from identical transgene constructs inserted at the same landing site in the genome, so that we could directly compare their effects on H3K27 trimethylation. Expression of either H3.3 or H3.3K27M at this late time in development had no effect on eye morphology (Figure 2C,D). Eye imaginal discs from wildtype larvae show similar staining of H3K27 trimethylation in both the anterior and posterior differentiating regions (Figure 2I), and induction of a wildtype H3.3 transgene had no effect on this pattern (Figure 2J). In contrast, induction of the H3.3K27M oncohistone dramatically inhibits H3K27 trimethylation posterior to the morphogenetic furrow in the eye disc (Figure 2K).

Studies in mammalian cells have suggested that cells must progress through at least one cell cycle before K27M oncohistones can inhibit the EZH2 methyltransferase (Chan *et al,* 2013; Nagaraja *et al*, 2019). To determine if inhibition in Drosophila also requires cell proliferation, we induced the H3.3K27M transgene and co-induced the cyclin E inhibitor p21, which blocks the last S phase in the eye disc and arrests cell division (Ollman et al, 2000; Figure 2C,D,G). Strikingly, we observed that H3.3K27M expression in these arrested cells does not inhibit H3K27 trimethylation (Figure 2L,M). These experiments demonstrate that the H3.3K27M oncohistone is a potent inhibitor of H3K27 trimethylation, but is only effective in proliferating cells.

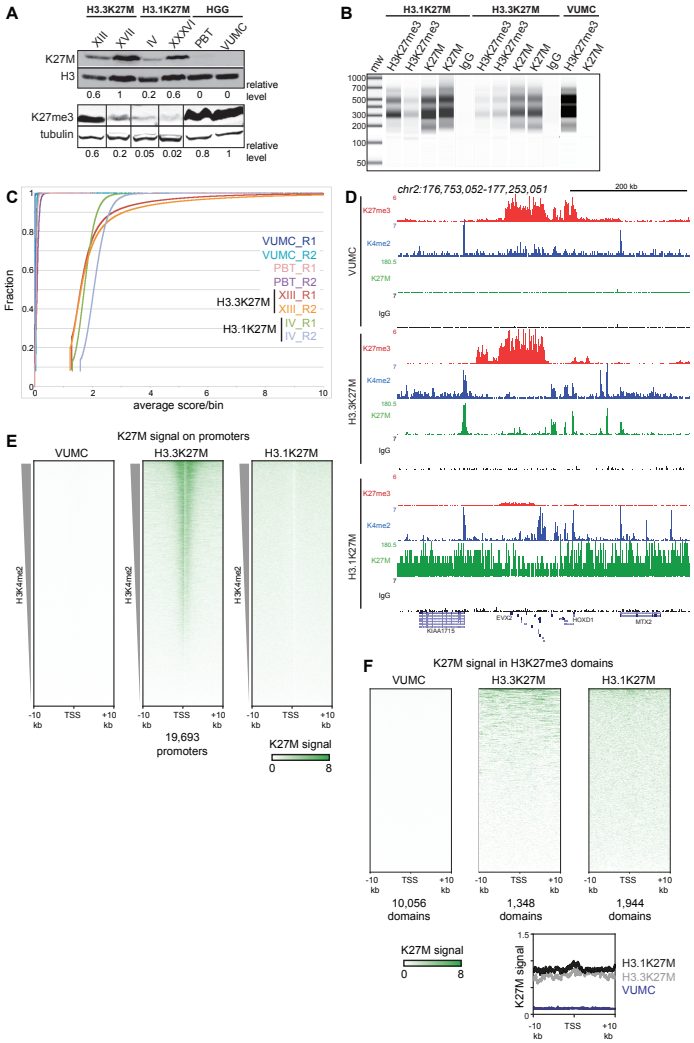

Figure 3. Global K27M distributions depend upon histone H3 types. (A) Western detection of K27M and H3K27me3 in glioma cell lines. K27M epitope amounts were normalized to histone H3 signal on the same blot, and H3K27me3 was normalized to tubulin on the same blot. The K27M histone is expressed over a range of levels in H3.1 and H3.3 mutant cell lines, but absent from VUMC and PBT gliomas. (B) Capillary electrophoresis of replicate CUT&RUN reactions. Antibody-targeted cleavage produce a nucleosomal ladder in amounts proportional to the amount of target epitope in samples. The H3 WT VUMC cell line is shown as a positive control for H3K27me3 and negative control for H3K27M. (C) Distribution graphs of read counts in 5 kb bins across the genome in glioma cell lines. H3.1K27M and H3.3K27M cells have moderate signal across the genome, while H3 wildtype VUMC and PBT cells have much lower counts, representing the very low non-specific background of H3K27M profiling. (D) Chromatin landscape of the silenced *HOXD* locus in glioma cell lines. All tracks are normalized by spike-in material to represent absolute amounts of signal. (E) Heat maps of H3K27M CUT&RUN signal on gene promoters in glioma cell lines. Promoters were ordered by the amount of CUT&RUN signal for H3K4me2, a mark of active transcription, in a 1 kb window around each TSS. The H3.3K27M cell line shows specific promoter enrichment of K27M in the most active promoters. (F) Heat maps of H3K27M across H3K27me3 domains in glioma cell lines. Domains were ordered by the amount of H3K27M signal. Both H3.1K27M and H3.3K27M cells show moderate K27M enrichment across domains. The average plot shows the enrichment of the K27M signal across the domains in each cell type.

Distinct K27M distributions in H3.1 and H3.3 mutant patient-derived cell lines

The genomic distribution of H3.3K27M has been previously mapped in DMG patient-derived cell lines (Piunti et al, 2017), however the distribution of H3.1K27M was not known. We therefore selected a set of well-characterized DMG cell lines to characterize their epigenomes by CUT&RUN. Use of cell lines avoids the cellular heterogeneity of tumor samples that can confound chromatin profiling (Nagaraja et al, 2019). The monoclonal antibody we used to detect the K27M substitution reacts with the mutated residue in both H3.1 and in H3.3 histones (Venneti et al, 2014), and we therefore examined K27M oncohistone abundance and distribution in two H3.3K27M-carrying (SU-DIPG-XIII and SU-DIPG-XVII; "XIII" and "XVII") patient-derived cell lines, and in two H3.1K27M-carrying (SU-DIPG-IV and SU-DIPG-XXXVI; "IV" and "XXXVI") lines to compare the effects of histone subtypes.

We first confirmed that the K27M epitope was present in all four H3K27M oncohistone DMGs by Western blotting, with different amounts of oncohistone between lines (Figure 3A). In contrast, two high-grade glioma (HGG) cell lines (VUMC and PBT) with wild-type H3.1 and H3.3 genes show no detectable K27M signal, demonstrating the specificity of the anti-K27M antibody. The effects on abundance of H3K27me3 are not related to the amount of K27M oncohistone expressed (Figure 3A), but appear related to the oncohistone type. We then used the anti-K27M antibody to map distribution of the epitope across the genome in the panel of cell lines, using CUT&RUN chromatin profiling (Skene & Henikoff, 2017; Skene et al, 2018). CUT&RUN relies on binding of a specific antibody to chromosomal sites to tether a protein-A-micrococcal nuclease (pA-MNase) fusion protein in samples of unfixed cells. Subsequent activation of the nuclease cleaves DNA around the binding sites with high specificity and sensitivity. Cleavage at antibody-targeted chromatin can be detected as nucleosomal fragments released from cells after nuclease activation, and we observed abundant fragments released from both H3.3K27M- and H3.1K27M-bearing cell lines (Figure 3B). In contrast, there is no detectable DNA released from VUMC cells, which express wildtype H3.1 and H3.3 histones, or from cells incubated with a control IgG antibody, indicating that the CUT&RUN reactions specifically cleave chromatin containing K27M oncohistones.

We focused on the results from one of each line with H3.1 (SU-DIPG-IV) or H3.3 (SU-DIPG-XIII) K27M mutations, as results for each pair of lines were very similar (see reproducibility in Figure 3 – figure supplement 1A,B and Figure 3 – figure supplement 2). CUT&RUN profiling of the K27M epitope showed moderate signal across the genome in both H3.1K27M and H3.3K27M lines (Figure 3C). This genome-wide signal is absent in cells lacking K27M oncohistones, and thus represents oncohistone that is broadly distributed. In addition, the XIII H3.3K27M line displayed 7,411 distinct peaks (Supplementary File 1). Notably, many of these peaks correspond to promoters, and overall these promoters are substantially enriched for K27M signal (Figure 3E). These peaks indicate that the H3.3K27M oncohistone is incorporated at sites of active histone turnover, superimposed upon a genome-wide background signal. To confirm that these peaks correspond to active sites, we generated profiles for the

histone H3K4me2 modification – a marker of active chromatin – in H3.3K27M cells. Indeed, 44% of the K27M oncohistone peaks fall precisely at called peaks of H3K4me2 (Supplementary File 1). Many K27M peaks coincide with the promoters of actively transcribed genes in DMGs, including *SOX2*, *OLIG2*, *MYC* and *GFAP* (Supplementary File 2), and the K27M signal has a moderate correlation (R^2=0.3) with gene expression measured by RNA-seq in these cells (Figure 3 – figure supplement 3; Nagaraja *et al,* 2017). In contrast, no H3K27M signal is observed in HGG lines with wildtype H3.3 histones (Figure 3D,E).

The distribution of K27M in H3.1K27M-bearing cell lines is quite different. Whereas H3K27M-targeted CUT&RUN released abundant amounts of nucleosome-sized DNA (Figure 3B) and 4-8 million fragments were sequenced and mapped, these reads are uniformly distributed across the genome for each of the two H3.1K27M-bearing cell lines (Figure 3C). Additionally, we found that H3K27M signal did not aggregate into defined peaks, and was not enriched over promoters (Figure 3E) or over H3K4me2 peaks (Supplementary File 1). Thus, we conclude that while both H3.1 and H3.3 K27M mutations result in the incorporation of the H3K27M epitope into chromatin, the distributions of the two oncohistones are consistent with replication-coupled histone deposition for both H3.1 and H3.3 oncohistones, and additional replication-independent deposition of H3.3K27M at active sites. Finally, we noted that the widespread K27M signal in both H3.1K27M and H3.3K27M lines is present in H3K27me3 domains (Figure 3F).

H3K27 trimethylation is globally reduced in H3.1K27M-bearing cell lines

The K27M epitope inhibits the H3K27 methyltransferase EZH2 *in vitro*, in cell culture, and in H3.3K27M-bearing cell lines (Castel et al, 2015; Funato & Tabar, 2018; Mohammad & Helin, 2017). Indeed, Western blotting for H3K27me3 shows very low levels of this histone modification in cell lines with both H3.3 and H3.1 K27M mutant cells (Figure 3A). However, as these two mutant cell lines have very different distributions of H3K27M oncohistone, we compared their genomic profiles of H3K27me3. Since the H3K27me3 epitope is conserved between Drosophila and humans, we used a fixed ratio of *Drosophila* S2 cells to human cells as a spike-in control. Normalization of human read counts by *Drosophila* read counts then allows direct comparison between samples. The validity of this spike-in approach is demonstrated by the linear relationship between read counts when varying the ratio of Drosophila and human cells in a H3K27me3 CUT&RUN reaction (Supplementary File 3).

Track browsing showed high signals for H3K27me3 in H3.3K27M cells at canonical silenced domains, such as the *HOXD* locus (Figure 3C), as previous studies have also shown (Piunti et al, 2017; Harutyunyan et al, 2019). However, it is apparent that H3K27me3 is greatly reduced at the *HOXD* locus in H3.1K27M-bearing cells. Strikingly, it is also apparent that many methylation domains present in VUMC cells are lacking in H3.3K27M cells. To analyze differences between cell lines more thoroughly, we defined differentially methylated chromatin domains between the H3.1K27M (SU-DIPG-IV), H3.3K27M (SU-DIPG-XIII), and histone-wildtype (VUMC-10) glioma lines. Unsupervised clustering of these variable H3K27me3 domains generated four major groups (Figure 4A, Supplementary File 1). The largest clusters (Clusters I-II) comprise 17,534 domains which are present in VUMC cells but absent in H3.3K27M cells, including numerous tissue-specific transcription factors. The remaining two clusters include regions where H3K27me3 is present in H3.3K27M cell lines. Cluster III includes 156 domains that are found both in VUMC and in H3.3K27M cells, and encompass genes that are typically silenced in many cell types, including those for the *CDKN2A* cell cycle inhibitor, the *WT1* tumor suppressor, and the *HOXD* transcription factors. Finally, cluster IV contains 1,380 domains that are absent in VUMC cells but present in H3.3K27M cells, including many critical regulators of developmental processes (Supplementary File 4). Thus, while H3.3K27M cells do have some H3K27 methylated domains, they are distinguished from other high-grade gliomas by the lack of a large number of H3K27me3 domains across the genome.

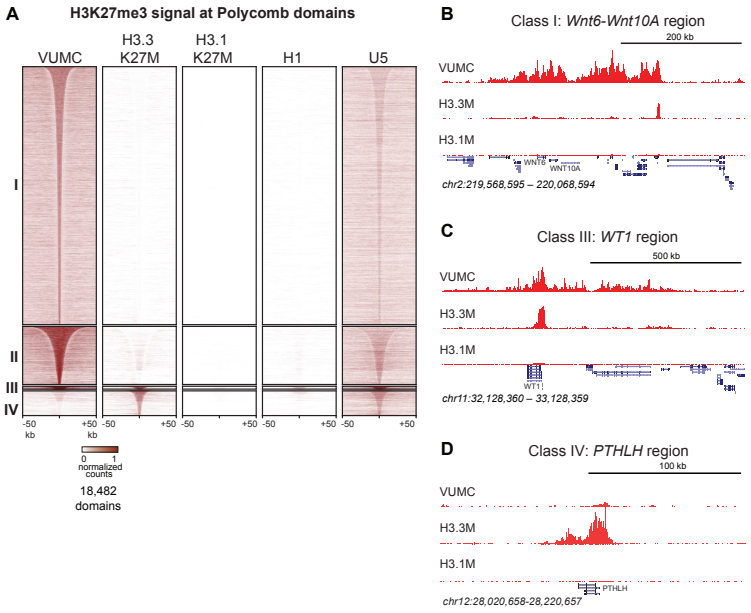

Figure 4. Shared and distinct H3K27me3 domains in K27M histone-expressing cells. (A) Heat maps of Drosophila-normalized H3K27me3 domains in glioma, embryonic stem cell (H1) and neural stem cell (U5) cell lines. Domains that differ between VUMC, H3.3K27M and H3.1K27M cells were selected, and divided into four groups by *k-means* (k=4) clustering. H3K27me3 signal across these regions was then plotted for H1 ESC and an NSC lines. Clusters I and II contain domains most enriched in VUMC and NSC lines. Cluster III contains heavily methylated domains that are present in all cell lines examined, although at low absolute levels in H3.1K27M cells. Cluster IV contains domains that are absent in VUMC cells but present to varying degrees in the other lines. (B) H3K27me3 landscape in a Cluster I region (present in VUMC but not in K27M histone mutant gliomas), encompassing the *WNT6* and *WNT10* oncogenes. (C) H3K27me3 landscape in a Cluster III region (present in VUMC and in H3.3K27M gliomas), encompassing the *WT1* tumor suppressor gene. (D) H3K27me3 landscape in a Cluster IV region (absent in VUMC but present in H3.3K27M gliomas), encompassing the *PTHLH* gene.

The reduction in domain numbers but not in H3K27 trimethylation levels across those domains (Figure 4) implies that EZH2 enzyme remains active in H3.3K27M-bearing cells. We

wondered if those domains remaining in H3.3K27M DMG cells corresponds to their developmental state. Indeed, DMG cells do express transcription factors of both pluripotency and differentiated cell types, suggesting developmental similarity to both stem cells and to differentiated cells (Filbin et al, 2018). To investigate this further, we profiled H3K27 trimethylation in primitive H1 embryonic stem cells and in an untransformed neural stem cell (NSC) line from fetal forebrain (Toledo et al, 2015). We then examined the enrichment of histone methylation across the differential domains we defined between VUMC and K27M mutant histone gliomas. We found that 5259 domains (21.3%) of the 24,733 domains found in U5 NSCs are found in VUMC cells, while only 1287 (5.20%) are shared with H3.3K27M cells. In contrast, 375 domains (26.8%) of 1401 domains in H1 ESCs are present in H3.3K27M-bearing cells. Additionally, both H3.3K27M and ES cells are distinctive in lacking H3K27 trimethylation from most Cluster I and II domains, and thus have a very limited global H3K27me3 profile.

Epigenomic changes are much more severe in H3.1K27M cells. These cells have very low bulk levels of H3K27 trimethylation, but domains can still be detected (Supplementary File 1), and cover many of the same regions found in H3.3K27M cells (Figure 4A, Clusters III and IV). These genomic patterns are consistent with other recent reports (Castel et al, 2018; Nagaraja *et al,* 2019). However, spike-in quantitation show that H3K27 trimethylation in these domains is reduced to 2-10% of the levels in VUMC or even in H3.3K27M cells (Figure 3C). Thus, the H3.3K27M and H3.1K27M oncohistones have dramatically different effects on Polycomb-regulated domains. This quantitative effect appears to be a conserved property of H3K27M mutant histones, as replication-coupled H3.2K27M oncohistones are more potent inhibitors of H3K27 trimethylation than H3.3K27M oncohistones in *C. elegans* (Delaney et al, 2019). We further genotyped these cell lines by targeted gene sequencing (Kuo *et al*, 2020), and identified multiple genetic alterations (Supplementary File 5), including biallelic deletions of the *CDKN2A* gene in the two H3.1K27M-bearing cell lines. This tumor suppessor gene is normally repressed by Polycomb silencing in normal cells, and suggests that inhibition of H3K27me3 by H3.1K27M requires secondary deletion of the *CDKN2A* locus for cell survival. In contrast, the *CDKN2A* locus is not typically altered in H3.3K27M-bearing cells (Piunti et al Nat Med 2017, Mohammed et al Nat Med 2017).

DMG cells maintain PRC2 targeting

H3K27M oncohistones have been suggested to trap the PRC2 complex on chromatin and inhibit activity of the EZH2 methyltransferase complex (Stafford et al, 2018; Fang *et al,* 2018). To investigate the relationship between PRC2 components, H3K27me3, and K27M mutant histones in chromatin, we profiled two Polycomb proteins – SUZ12 of the PRC2 complex and the MTF2 transcription factor – in VUMC and in K27M mutant glioma lines. Similar amounts of these proteins are present in all three gliomas (Figure 5 – figure supplement 1C). We detected thousands of sites for each subunit in each line (Supplementary File 1), with high concordance between biological replicates (Figure 3 – figure supplement 1). We then mapped SUZ12 and MTF2 signal in H3.3K27M glioma cells at sites of K27M enrichment (as H3.1K27M cells only have the K27M epitope dispersed across the genome). This analysis showed no enrichment of SUZ12 or MTF2 at active promoters with the K27M signal in H3.3K27M-bearing cells (Figure 5A; Figure 5 – figure supplement 2A,C). Similarly, K27M-defined peaks were not enriched for these PRC2 components (Figure 5 – figure supplement 2D).

To examine PRC2 localization at silenced domains, we mapped SUZ12 and MTF2 signals onto the H3K27me3 clusters for each cell line (Figure 4B). In VUMC glioma cells, both PRC2 components are enriched in Clusters I, II, and III, where H3K27me3 is also enriched (Figure 5A,B). The H3.3K27M line lacks H3K27 methylation in Clusters I and II, and PRC2 components are similarly lacking. In contrast, the H3K27me3-enriched regions in Clusters III and IV are enriched for both SUZ12 and MTF2 in H3.3K27M-bearing cells (Figure 5A,B). Thus, in both the VUMC and H3.3K27M glioma lines, H3K27me3 domains are co-occupied by PRC2.

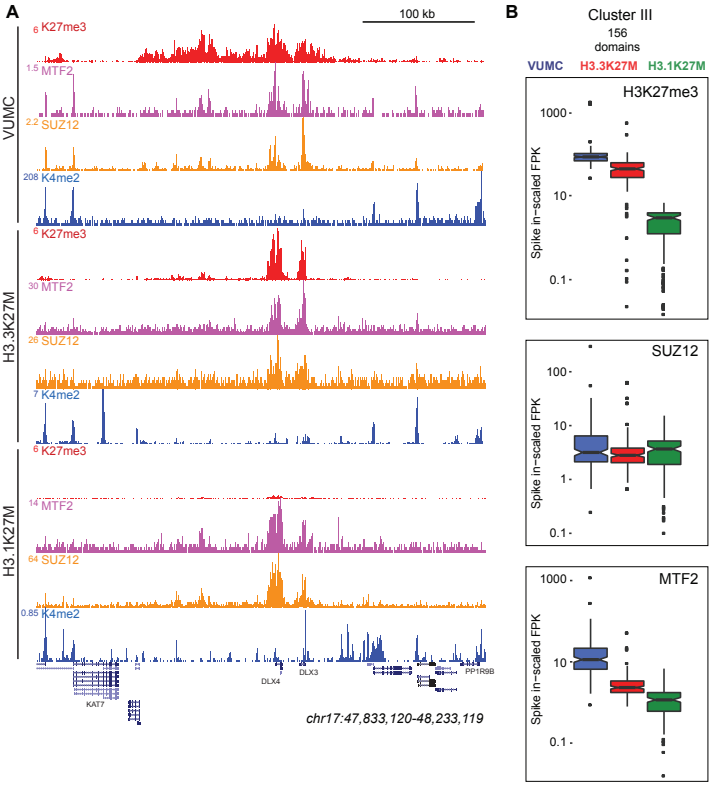

Figure 5. K27M histone-expressing cells maintain PRC2 binding. (A) Chromatin landscape around the *DLX3* gene for H3K27me3, H3K4me2, and Polycomb components in glioma cell lines. All three cell lines display binding of Polycomb components within the H3K27me3 domain. (B) Bar-and-whisker plots of H3K27me3, SUZ12, and MTF2 signals in shared Cluster III domains in VUMC, H3.3K27M (XIII), and H3.1K27M (IV) cell lines. H3K27me3 signal is similar between VUMC and H3.3K27M lines, but low in H3.1K27M cells. In contrast, the PRC2 subunit SUZ12 is similarly enriched in all three cell lines at these shared domains, while MTF2 enrichment varies between lines.

While H3.1K27M gliomas have dramatically reduced levels of H3K27me3 in domains, we find that those domains continue to be enriched for both SUZ12 and MTF2 proteins (Clusters III and IV, Figure 5A; Figure 5 – figure supplement 1).

We compared the spike-normalized levels of these proteins across Cluster III sites, which are H3K27me3 domains in all three cell lines, and found similar levels of SUZ12 and significant levels of MTF2 in all three cell lines in these domains (Figure 5B). These results imply that Polycomb proteins are correctly targeted in both H3.1K27M and H3.3K27M cells, but PRC2 must be strongly inhibited in H3.1K27M cells to account for their low H3K27me3 signal.

Discussion

Replication-coupled and -independent mechanisms of H3 variant deposition were first demonstrated almost two decades ago (Ahmad & Henikoff, 2002) but the roles of these different deposition mechanisms in H3.1-and H3.3-mutant gliomagenesis are not known. We use a panel of high-grade glioma and DMG cell lines to profile the genome-wide localizations of K27M oncohistones. Previous reports for the localization of H3.1K27M have been contradictory, identifying accumulation at active promoters (Piunti et al, 2017) or more broadly throughout the genome (Nagaraja *et al,* 2019). Our results confirm that H3.1K27M is deposited throughout the genome, consistent with replication-coupled deposition of H3.1, while H3.3K27M accumulates primarily at sites of histone turnover but also at low levels genome-wide, probably through replication-coupled deposition. Furthermore, quantitative profiling demonstrates that H3K27me3 is much lower in H3.1K27M- than in H3.3K27M-bearing cells, although neither the H3.1K27M nor H3.3K27M oncohistones appear to trap or prevent PRC2 binding to chromatin.

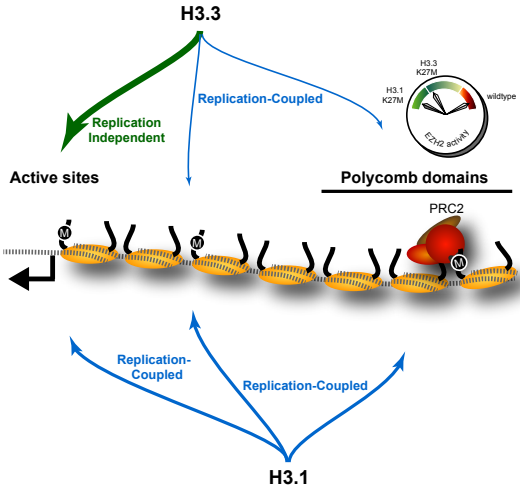

Figure 6. The effect of K27M histones is determined by histone deposition pathways and the distribution of PRC2 complexes on chromatin. Nucleosomes (yellow) are assembled from new histones by Replication-Coupled (blue arrows) and Replication-Independent (green arrow) pathways. Most H3.3 histones are bound by variant-specific chaperones and incorporated at active sites and promoters by Replication-Independent pathways, but a small amount of H3.3 histones are incorporated during DNA replication throughout the genome. The H3.1 histone is exclusively used for Replication-Coupled assembly, and so deposited throughout the genome at higher levels. Thus, H3.1K27M mutants incorporate high levels of the K27M ('M') epitope in Polycomb domains, where it binds and inhibits the histone methyltransferase activity of the PRC2 complex. In contrast, most K27M epitope in H3.3K27M mutants is incorporated at active sites far from Polycomb domains, resulting in weaker inhibition of PRC2 in these cells.

Competing models have suggested that H3K27M oncohistones sequester (Fang et al, 2018) or poison (Lee et al, 2019) PRC2. Further, it has been suggested that these effects occur either on chromatin or in solution (Nagaraja *et al,* 2019). However, PRC2 components in DMG cells do not coincide with the bulk of K27M oncohistones in these cells. Taken together, our human and fly results provide a coherent model for inhibition by H3K27M oncohistones (Figure 6). We have demonstrated that the K27M epitope only inhibits H3K27 trimethylation on chromatin *in vivo*, supporting the idea that these oncohistones inhibit chromatin-bound PRC2 complexes. A possible mechanism comes from recent reports showing that EZH2 methylates itself, and that this automethylation is required for full catalytic activity (Lee et al, 2019; Wang et al, 2019). These studies also showed that H3K27M blocks EZH2 automethylation, and might contribute to the dominant effect of H3K27M mutations.

Our results imply that H3K27M oncohistones inhibit the EZH2 methyltransferase at its chromatin binding sites within Polycomb-regulated domains. A critical time for maintaining epigenomic patterns is during S phase of the cell cycle, when histone modifications must be established on newly assembled nucleosomes behind the replication fork (Alabert et al, 2015). It is striking that H3K27M oncohistones inhibit H3K27 trimethylation only in proliferating cells (Chan et al 2013; Nagajara et al 2019). Existing H3K27me3 levels generally remain stable in the absence of DNA replication (Jadhav et al 2020), thus EZH2 activity is only needed in cycling cells. Perhaps new H3K27M oncohistones deposited behind the replication fork inhibit the EZH2 methyltransferase, thereby blocking re-establishment of H3K27me3 domains. In this model, only H3K27M oncohistones that undergo replication-coupled deposition near the sites of PRC2 recruitment are toxic to EZH2 activity. As H3.1K27M oncohistones are deposited throughout the genome, PRC2 poisoning in these cells eliminates H3K27 trimethylation genome-wide. In contrast, the less potent effect of H3.3K27M oncohistones on H3K27 trimethylation in DMG cells may be due to the smaller fraction of H3.3K27M oncohistones that undergo replication-coupled deposition, as most of this oncohistone is sequestered at active promoters far from H3K27me3 domains. The finding that human histone H3.3 localize over replication foci in early-S-phase cells (Ray-Gallet et al, 2011; Clement et al, 2018) is consistent with our model.

That only H3K27M oncohistones deposited during DNA replication are toxic to EZH2 activity also explains why particular secondary mutations are associated with either H3.1K27M- or H3.3K27M-bearing gliomas. For example, H3.3K27M but not H3.1K27M gliomas have a significantly increased frequency of ATRX mutations (Khuong-Quang *et al,* 2012; Mackay *et al*, 2017). ATRX is a chromatin remodeler involved in alternative telomere lengthening pathways in some cells (Heaphy *et al,* 2011), but also mediates replication-independent histone deposition (Goldberg et al, 2010). Thus, we expect that ATRX mutations may enhance the amount of H3.3K27M oncohistones deposited during DNA replication, thereby increasing inhibitory effects on H3K27 trimethylation. Similarly, *CDKN2A* loss in H3.1K27M-bearing cells suggests that this oncohistone requires different secondary mutations to compensate for the loss of Polycomb silencing at tumor suppressor genes. Such a dependency would explain why

H3.1K27M mutations are more rare than H3.3 ones. A therapeutic corollary is that H3.1 and H3.3 oncohistones may confer distinct cellular sensitivities to chromatin modification inhibitors, either by affecting chromatin silencing or by affecting histone deposition pathways, thereby reshaping epigenomic landscapes.

Materials and Methods

Biological materials

Cell lines: Patient-derived K27M SU-DIPG-IV (IV, H3.1K27M), SU-DIPG-XXXVI (XXXVI, H3.1K27M), SU-DIPG-XIII (XIII, H3.3K27M) and SU-DIPG-XVII (XVII, H3.3K27M) cell lines were generously provided by the laboratory of M. Monje (Stanford University) and have been previously described (Grasso et al, 2015). The high grade glioma (HGG) cell line with wildtype histone genes VUMC-DIPG-10 (VUMC) (Meel et al, 2017) was obtained through a materials transfer agreement with Esther Hulleman (VU University Medical Center, Amsterdam, Netherlands), and generation of PBT-04 was reported previously (PBT; Brabetz et al, 2018). The H1 ESC line was obtained from WiCell (Madison WI). The U5 neural stem cell (NSC) line (Toledo et al, 2015) was obtained from PJ Paddison (FHCRC, Seattle WA). Drosophila S2 cells were obtained from ThermoFisher. The patient-derived glioma cell lines harboring H3K27M mutations (SU-DIPG-IV, SU-DIPG-XIII, SU-DIPG-XVII, SU-DIPG-XXXVI) were generously provided by Dr. Michelle Monje and had targeted sequencing to confirm H3 mutational status. PBT-04 was generated by the Olson Laboratory and maintained as described previously (Braebetz et al., 2018). VUMC-10 was generously provided directly by Dr. E. Huelleman. Mycoplasma testing was performed every 3 months with the MycoProbe mycoplasma detection kit from R&D systems (Minneapolis, MN). None of the cell lines used in this study are found on the misidentified cell lines list from the International Cell Line Authentication Committee.

Fly lines and crosses: The *GMR-GAL4-D* driver (Ahmad & Henikoff, 2001b), *UASp-H3.3K27M* (Ahmad & Spens, 2019), and *GMR-p21* (Ollman et al, 2000) lines were used. All crosses were performed at 25˚C. Crawling 3rd instar larvae were selected, and eye discs were dissected and fixed in 4% paraformaldehyde/PBST (PBS with 0.1% triton-X100). Fixed tissues were blocked with 10% goat serum/PBST, and incubated with primary antiserum at 4˚ overnight, and with fluorescently-labeled secondary antibodies (1:200 dilution, Jackson ImmunoResearch). All tissues were stained with 0.5 µg/mL DAPI/PBS, mounted in 80% glycerol on slides, and imaged by epifluorescence on an EVOS FL Auto 2 inverted microscope (Thermo Fisher Scientific) with a 10X or 20X objective. Pseudo-colored images were adjusted and composited in Adobe Photoshop and Adobe Illustrator. H3K27me3 signal in the anterior and posterior portions of eye discs was measured as the mean value in a 100 pixel x 100 pixel box using Photoshop.

Plasmid constructs: We built plasmids by Gibson assembly for constitutive expression of histones and K27M mutant histones tagged at their C-termini with 2XFLAG epitope tags using the *Copia* promoter from the plasmid pCoPURO (Addgene 17533), and Drosophila H3 and H3.3 histones from previously published constructs (Ahmad & Henikoff, 2002). Site-directed mutagenesis was used to introduce K27M substitutions into the H3 and H3.3 genes. To make histone tail constructs, we made a Copia-H3-RFP fusion construct and then used site-directed mutagenesis to delete the histone fold domain. All plasmids were confirmed by Sanger sequencing of the fusion gene. The following plasmids are used here: pCoH3_FLAG, pCoH3K27M_FLAG, pCoH3.3_FLAG, pCoH3.3K27M_FLAG, pCoH3tail_RFP, and pCoH3K27Mtail_RFP.

Cell Culture

Human cells were grown in NeuroCult medium (StemCell Technologies, Vancouver, BC) supplemented with human-EGF at 20 ng/mL and human-bFGF at 20 ng/mL supplemented with penicillin/streptomycin. Cells were passaged with Accutase for dissociation. Drosophila S2 cells were grown to log phase in HYQ-SFX insect medium (ThermoFisher) supplemented with 18 mM L-Glutamine and harvested by scraping. Drosophila cells were transiently lipofected with plasmid constructs using Fugene HD (Promega), grown for 2 days, then spun onto glass slides in a Cytospin centrifuge (Thermo), fixed, and immunostained as described (Ahmad & Henikoff, 2001a). Nuclei were photographed using an EVOS FL Auto 2 inverted microscope (ThermoFisher) with a 20X lens. Two transfections were performed for each experiment. Nuclei were scored for transfection by the construct marker (RFP or FLAG), and the mean signal of H3K27me3 staining was measured for 50 un-transfected and 50 transfected nuclei in the DAPI-stained nucleus using Photoshop CS6 Extended for each construct. Signals were corrected for background on slides and then divided by the brightest H3K27me3-stained nucleus to normalize between slides and images.

Western Blotting

For histone Western blots, 10^6 cells were pelleted, washed once with PBS and resuspended in 200 µL standard protein sample buffer to make whole cell extracts. Samples were vortexed, boiled for 5 minutes, then cooled to room temperature. Benzonase (1 µL) was added and samples were incubated at room temperature for 5 minutes before freezing for further use. For SUZ12 and MTF2, chromatin fractions were isolated using acid extraction. Samples were run on 4-20% Tris-Glycine polyacrylamide gels (Invitrogen), transferred to nitrocellulose membrane and 1:1000 dilutions of primary and secondary antibodies were used for blotting. SUZ12 was probed first and the same blot was stripped with Stripping Buffer (LiCor, Lincoln, NE) and then probed with anti-MTF2. Secondary goat anti-mouse IRDye800CW and goat anti-rabbit IRDye680LT (LI-COR, Lincoln, NE) were used and quantification was performed using the ImageJ software, accounting for local background and with internal loading control.

CUT&RUN chromatin profiling

CUT&RUN was performed as described (Skene et al, 2018). All antibodies were used at 1:100 dilutions, except anti-SUZ12 and anti-MTF2, which were used at 1:50. Cells were counted using a ViCell (ThermoFisher), and spike-in CUT&RUN was performed with a 1:20 ratio of Drosophila S2 cells to human cells (50,000 S2 cells to 1,000,000 human cells) in each reaction.

Library Preparation and Sequencing

Extracted DNA was subjected to the KAPA Hyper-prep library preparation kit protocol (Roche,
Inc.) and amplified as previously described (Skene & Henikoff, 2017), with the modification that the end-repair reaction and poly-A tailing reactions were performed at 60˚C to preserve small fragments, as described (Liu et al, 2018). Sequencing reads were

mapped to the human hg19 genome build and the genome build for the relevant spike-in for each dataset (Drosophila dm6 for H3K27me3, Saccharomyces cerevisiae R64-1-1 for K27M, or E. coli Ensembl genome build for SUZ12 and MTF2) using Bowtie2 (Langmead &Salzberg*, 2012*), and paired-end fragment bed files and spike-normalized bedgraphs generated using bedtools (Quinlan & Hall, 2010). Spike-normalization factors were calculated by dividing 10,000 by the number of spike-in reads mapped, and for each sample the bedgraph signal was multiplied by the corresponding factor.

Data Analysis

Correlation heatmaps were generated in R (https://www.rproject.org), using normalized fragment counts mapping to 10 kb windows spanning the hg19 genome. Peaks were called using SEACR (Meers et al, 2019). For datasets for which biological replicates were available, peak lists from two replicates were merged using the bedops merge (-m) utility (Neph et al, 2012). For genome-wide assessment of CUT&RUN signal, we used deeptools2 to sum basepair counts in 5 kb bins, and plotted the ranked counts in MS Excel. Differential H3K27me3 regions used for K-means clustering were generated as follows: 1) We used the bedops partition (-p) utility to determine unique overlapping segments between merged H3K27me3 peak lists from VUMC, XIII, and IV datasets; 2) From the partitioned peak list, for any two partitioned regions that were directly adjacent to one another, we filtered out any that were less than 10 kb in length, in order to select only the "dominant" segment in each region of partitioning overlaps, and to avoid doubly mapping adjacent partitioned regions; 3) For all other free-standing regions, we filtered out any that were less than 3 kb in length. This resulted in 18,482 regions used for clustering. K-means clustering was carried out using the "kmeans" utility in R. Four clusters were selected as the optimal cluster solution based on selecting the "knee" of the curve in a plot of the number of clusters vs. within-cluster distance, tested across all possible solutions between 2 and 15 clusters. Overlaps between cluster regions and gene promoters, and mapping of H3K27me3, SUZ12 and MTF2 fragments to cluster III regions in Figure 5B, were ascertained using the bedtools intersect utility (Quinlan & Hall, 2010). Fragments mapped to cluster III in Figure 5B were first scaled by fragments per kilobase (1000/length of region), and then by a scaling constant that is inversely proportional to the number of spike in reads mapped (VUMC-H3K27me3: 0.786, SUDIPG-XIII-H3K27me3: 0.292, SUDIPG-IV-H3K27me3: 0.046, VUMC-SUZ12: 0.104, SUDIPG-XIII-SUZ12: 0.385, SUDIPG-IV-SUZ12: 0.185, VUMC-MTF2: 0.244, SUDIPG-XIII-MTF2: 0.333, SUDIPG-IV-MTF2: 0.084). Detailed positional information for all merged peak calls used in this manuscript are found in Supplementary File 1. CUT&RUN signal heatmaps, gene plots, and average plots were generated using deeptools (Ramirez et al, 2014). RNA-seq data for SU-DIPG-XIII was obtained from GSM2471870 (https://www.ncbi.nlm.nih.gov/geo/query/acc.cgi?acc=GSM2471870). For comparison of RNA-seq counts with H3K27M CUT&RUN in SUDIPG-XIII, CUT&RUN reads were mapped in a 10kb window surrounding hg19 TSSs. Datasets were visualized using the UCSC Genome Browser. Boxplots were generated with the web application BoxPlotR (http://shiny.chemgrid.org/boxplotr/).

References

Ahmad K, Henikoff S. (2001a). Centromeres are specialized replication domains in heterochromatin. *J Cell Biol* **153:**101-10. PubMed PMID: 11285277.

Ahmad K, Henikoff S. (2001b). Modulation of a transcription factor counteracts heterochromatic gene silencing in Drosophila. *Cell* **104:**839-47. PubMed PMID: 11290322.

Ahmad K, Henikoff S. (2002). The histone variant H3.3 marks active chromatin by replication-independent nucleosome assembly. *Mol Cell* **9:**1191-200. PubMed PMID: 12086617.

Ahmad K, Spens AE. (2019). Separate Polycomb Response Elements control chromatin state and activation of the vestigial gene. *PLoS Genet* **15:**e1007877. doi: 10.1371/journal.pgen.1007877. PubMed PMID: 31425502.

Alabert C, Barth TK, Reverón-Gómez N, Sidoli S, Schmidt A, Jensen ON, Imhof A, Groth A. (2015). Two distinct modes for propagation of histone PTMs across the cell cycle. *Genes Dev* **29:**585-90. doi: 10.1101/gad.256354.114. PubMed PMID: 25792596.

Bender S, Tang Y, Lindroth AM, Hovestadt V, Jones DT, Kool M, Zapatka M, Northcott PA, Sturm D, Wang W, Radlwimmer B, Højfeldt JW, Truffaux N, Castel D, Schubert S, Ryzhova M, Seker-Cin H, Gronych J, Johann PD, Stark S, Meyer J, Milde T, Schuhmann M, Ebinger M, Monoranu CM, Ponnuswami A, Chen S, Jones C, Witt O, Collins VP, von Deimling A, Jabado N, Puget S, Grill J, Helin K, Korshunov A, Lichter P, Monje M, Plass C, Cho YJ, Pfister SM. (2013). Reduced H3K27me3 and DNA hypomethylation are major drivers of gene expression in K27M mutant pediatric high-grade gliomas. *Cancer Cell* **24:**660-72. doi: 10.1016/j.ccr.2013.10.006. PubMed PMID: 24183680.

Brabetz S, Leary SES, Gröbner SN, Nakamoto MW, Şeker-Cin H, Girard EJ, Cole B, Strand AD, Bloom KL, Hovestadt V, Mack NL, Pakiam F, Schwalm B, Korshunov A, Balasubramanian GP, Northcott PA, Pedro KD, Dey J, Hansen S, Ditzler S, Lichter P, Chavez L, Jones DTW, Koster J, Pfister SM, Kool M, Olson JM. (2018). A biobank of patient-derived pediatric brain tumor models. *Nat Med* **24:**1752-1761. doi: 10.1038/s41591-018-0207-3. PubMed PMID: 30349086.

Castel D, Philippe C, Calmon R, Le Dret L, Truffaux N, Boddaert N, Pagès M, Taylor KR, Saulnier P, Lacroix L, Mackay A, Jones C, Sainte-Rose C, Blauwblomme T, Andreiuolo F, Puget S, Grill J, Varlet P, Debily MA. (2015). Histone H3F3A and HIST1H3B K27M mutations define two subgroups of diffuse intrinsic pontine gliomas with different prognosis and phenotypes. *Acta Neuropathol* **130:**815-27. doi: 10.1007/s00401-015-1478-0. PubMed PMID: 26399631.

Castel D, Philippe C, Kergrohen T, Sill M, Merlevede J, Barret E, Puget S, Sainte-Rose C, Kramm CM, Jones C, Varlet P, Pfister SM, Grill J, Jones DTW, Debily MA. (2018). Transcriptomic and epigenetic profiling of 'diffuse midline gliomas, H3 K27M-mutant'

discriminate two subgroups based on the type of histone H3 mutated and not supratentorial or infratentorial location. *Acta Neuropathol Commun* **6:**117. doi: 10.1186/s40478-018-0614-1. PubMed PMID: 30396367.

Chan KM, Fang D, Gan H, Hashizume R, Yu C, Schroeder M, Gupta N, Mueller S, James CD, Jenkins R, Sarkaria J, Zhang Z. (2013). The histone H3.3K27M mutation in pediatric glioma reprograms H3K27 methylation and gene expression. *Genes Dev* **27:**985-90. doi: 10.1101/gad.217778.113. PubMed PMID: 23603901.

Clement C, Orsi GA, Gatto A, Boyarchuk E, Forest A, Hajj B, Mine-Hattab J, Garnier M, Gurard-Levin ZA, Quivy J-P, Almouzni G (2018). High-resolution visualization of H3 variants during replication reveals their controlled recycling. Nat Commun **9:**3181. PMID: 30093638.

Delaney K, Strobino M, Wenda JM, Pankowski A, Steiner FA. (2019). H3.3K27M-induced chromatin changes drive ectopic replication through misregulation of the JNK pathway in C. elegans. *Nat Commun* **10:**2529. doi: 10.1038/s41467-019-10404-9. PubMed PMID: 31175278.

Drané P, Ouararhni K, Depaux A, Shuaib M, Hamiche A. (2010). The death-associated protein DAXX is a novel histone chaperone involved in the replication-independent deposition of H3.3. *Genes Dev* **24:**1253-65. doi: 10.1101/gad.566910. PubMed PMID: 20504901.

Fang D, Gan H, Cheng L, Lee JH, Zhou H, Sarkaria JN, Daniels DJ, Zhang Z. (2018). H3.3K27M mutant proteins reprogram epigenome by sequestering the PRC2 complex to poised enhancers. *Elife* **7.** *pii:* e36696. doi: 10.7554/eLife.36696. PubMed PMID: 29932419.

Filbin MG, Tirosh I, Hovestadt V, Shaw ML, Escalante LE, Mathewson ND, Neftel C, Frank N, Pelton K, Hebert CM, Haberler C, Yizhak K, Gojo J, Egervari K, Mount C, van Galen P, Bonal DM, Nguyen QD, Beck A, Sinai C, Czech T, Dorfer C, Goumnerova L, Lavarino C, Carcaboso AM, Mora J, Mylvaganam R, Luo CC, Peyrl A, Popović M, Azizi A, Batchelor TT, Frosch MP, Martinez-Lage M, Kieran MW, Bandopadhayay P, Beroukhim R, Fritsch G, Getz G, Rozenblatt-Rosen O, Wucherpfennig KW, Louis DN, Monje M, Slavc I, Ligon KL, Golub TR, Regev A, Bernstein BE, Suvà ML. (2018). Developmental and oncogenic programs in H3K27M gliomas dissected by single-cell RNA-seq. *Science* **360:**331-335. doi: 10.1126/science.aao4750. PubMed PMID: 29674595.

Fontebasso AM, Papillon-Cavanagh S, Schwartzentruber J, Nikbakht H, Gerges N, Fiset PO, Bechet D, Faury D, De Jay N, Ramkissoon LA, Corcoran A, Jones DT, Sturm D, Johann P, Tomita T, Goldman S, Nagib M, Bendel A, Goumnerova L, Bowers DC, Leonard JR, Rubin JB, Alden T, Browd S, Geyer JR, Leary S, Jallo G, Cohen K, Gupta N, Prados MD, Carret AS, Ellezam B, Crevier L, Klekner A, Bognar L, Hauser P, Garami M, Myseros J, Dong Z, Siegel PM, Malkin H, Ligon AH, Albrecht S, Pfister SM, Ligon KL, Majewski J, Jabado N, Kieran MW. (2014). Recurrent somatic mutations in ACVR1 in pediatric midline high-grade astrocytoma. *Nat Genet* **46:**462-6. doi: 10.1038/ng.2950. PubMed PMID: 24705250.

Funato, K, Tabar, V (2018). Histone Mutations in Cancer. *Annual Review of Cancer Biology* **2:**337-351.

Goldberg AD, Banaszynski LA, Noh KM, Lewis PW, Elsaesser SJ, Stadler S, Dewell S, Law M, Guo X, Li X, Wen D, Chapgier A, DeKelver RC, Miller JC, Lee YL, Boydston EA, Holmes MC, Gregory PD, Greally JM, Rafii S, Yang C, Scambler PJ, Garrick D, Gibbons RJ, Higgs DR, Cristea IM, Urnov FD, Zheng D, Allis CD. (2010). Distinct factors control histone variant H3.3 localization at specific genomic regions. *Cell* **140:**678-91. doi: 10.1016/j.cell.2010.01.003. PubMed PMID: 20211137.

Grasso CS, Tang Y, Truffaux N, Berlow NE, Liu L, Debily MA, Quist MJ, Davis LE, Huang EC, Woo PJ, Ponnuswami A, Chen S, Johung TB, Sun W, Kogiso M, Du Y, Qi L, Huang Y, Hütt-Cabezas M, Warren KE, Le Dret L, Meltzer PS, Mao H, Quezado M, van Vuurden DG, Abraham J, Fouladi M, Svalina MN, Wang N, Hawkins C, Nazarian J, Alonso MM, Raabe EH, Hulleman E, Spellman PT, Li XN, Keller C, Pal R, Grill J, Monje M. (2015). Functionally defined therapeutic targets in diffuse intrinsic pontine glioma. *Nat Med* **21:**555-9. doi: 10.1038/nm.3855. PubMed PMID: 25939062.

Harutyunyan AS, Krug B, Chen H, Papillon-Cavanagh S, Zeinieh M, De Jay N, Deshmukh S, Chen CCL, Belle J, Mikael LG, Marchione DM, Li R, Nikbakht H, Hu B, Cagnone G, Cheung WA, Mohammadnia A, Bechet D, Faury D, McConechy MK, Pathania M, Jain SU, Ellezam B, Weil AG, Montpetit A, Salomoni P, Pastinen T, Lu C, Lewis PW, Garcia BA, Kleinman CL, Jabado N, Majewski J. (2019). H3K27M induces defective chromatin spread of PRC2-mediated repressive H3K27me2/me3 and is essential for glioma tumorigenesis. *Nat Commun* **10:**1262. doi: 10.1038/s41467-019-09140-x. PubMed PMID: 30890717.

Heaphy CM, de Wilde RF, Jiao Y, Klein AP, Edil BH, Shi C, Bettegowda C, Rodriguez FJ, Eberhart CG, Hebbar S, Offerhaus GJ, McLendon R, Rasheed BA, He Y, Yan H, Bigner DD, Oba-Shinjo SM, Marie SK, Riggins GJ, Kinzler KW, Vogelstein B, Hruban RH, Maitra A, Papadopoulos N, Meeker AK. (2011). Altered telomeres in tumors with ATRX and DAXX mutations. *Science* **333:**425. doi: 10.1126/science.1207313. PubMed PMID: 21719641.

Herz HM, Morgan M, Gao X, Jackson J, Rickels R, Swanson SK, Florens L, Washburn MP, Eissenberg JC, Shilatifard A. (2014). Histone H3 lysine-to-methionine mutants as a paradigm to study chromatin signaling. *Science* **345:**1065-70. doi: 10.1126/science.1255104. PubMed PMID: 25170156.

Justin N, Zhang Y, Tarricone C, Martin SR, Chen S, Underwood E, De Marco V, Haire LF, Walker PA, Reinberg D, Wilson JR, Gamblin SJ. (2016). Structural basis of oncogenic histone H3K27M inhibition of human polycomb repressive complex 2.

Nat Commun **7:**11316. doi: 10.1038/ncomms11316. PubMed PMID: 27121947.

Khuong-Quang DA, Buczkowicz P, Rakopoulos P, Liu XY, Fontebasso AM, Bouffet E, Bartels U, Albrecht S, Schwartzentruber J, Letourneau L, Bourgey M, Bourque G, Montpetit A, Bourret G, Lepage P, Fleming A, Lichter P, Kool M, von Deimling A, Sturm D, Korshunov A, Faury D, Jones DT, Majewski J, Pfister SM, Jabado N, Hawkins C. (2012). K27M mutation in histone H3.3 defines clinically and biologically distinct subgroups of pediatric diffuse intrinsic pontine gliomas. *Acta Neuropathol* **124:**439-47. doi: 10.1007/s00401-012-0998-0. PubMed PMID: 22661320.

Kuo AJ, Paulson VA, Hempelmann JA, et al. (2020). Validation and implementation of a modular targeted capture assay for the detection of clinically significant molecular oncology alterations. *Pract Lab Med*. **19:**e00153. doi:10.1016/j.plabm.2020.e00153. PubMed PMID: 32123717.

Langmead B, Salzberg SL. (2012). Fast gapped-read alignment with Bowtie 2. *Nat Methods* **9:**357-9. doi: 10.1038/nmeth.1923. PubMed PMID: 22388286.

Lee CH, Yu JR, Granat J, Saldaña-Meyer R, Andrade J, LeRoy G, Jin Y, Lund P, Stafford JM, Garcia BA, Ueberheide B, Reinberg D. (2019). Automethylation of PRC2 promotes H3K27 methylation and is impaired in H3K27M pediatric glioma. *Genes Dev*
33:1428-1440. doi: 10.1101/gad.328773.119. PubMed PMID: 31488577.

Lehnertz B, Zhang YW, Boivin I, Mayotte N, Tomellini E, Chagraoui J, Lavallée VP, Hébert J, Sauvageau G. (2017). H3(K27M/I) mutations promote context-dependent transformation in acute myeloid leukemia with RUNX1 alterations. *Blood* **130:**2204-2214. doi: 10.1182/blood-2017-03-774653. PubMed PMID: 28855157.

Lewis PW, Müller MM, Koletsky MS, Cordero F, Lin S, Banaszynski LA, Garcia BA, Muir TW, Becher OJ, Allis CD. (2013). Inhibition of PRC2 activity by a gain-of-function H3 mutation found in pediatric glioblastoma. *Science* **340:**857-61. doi: 10.1126/science.1232245. PubMed PMID: 23539183.

Liu N, Hargreaves VV, Zhu Q, Kurland JV, Hong J, Kim W, Sher F, Macias-Trevino C, Rogers JM, Kurita R, Nakamura Y, Yuan GC, Bauer DE, Xu J, Bulyk ML, Orkin SH. (2018). Direct Promoter Repression by BCL11A Controls the Fetal to Adult Hemoglobin Switch. *Cell* **173:**430-442.e17. doi: 10.1016/j.cell.2018.03.016. PubMed PMID: 29606353.

Mackay A, Burford A, Carvalho D, Izquierdo E, Fazal-Salom J, Taylor KR, Bjerke L, Clarke M, Vinci M, Nandhabalan M, Temelso S, Popov S, Molinari V, Raman P, Waanders AJ, Han HJ, Gupta S, Marshall L, Zacharoulis S, Vaidya S, Mandeville HC, Bridges LR, Martin AJ, Al-Sarraj S, Chandler C, Ng HK, Li X, Mu K, Trabelsi S, Brahim DH, Kisljakov AN, Konovalov DM, Moore AS, Carcaboso AM, Sunol M, de Torres C, Cruz O, Mora J, Shats LI, Stavale JN, Bidinotto LT, Reis RM, Entz-Werle N, Farrell M, Cryan J, Crimmins D, Caird J, Pears J, Monje M, Debily MA, Castel D, Grill J, Hawkins C, Nikbakht H, Jabado N, Baker SJ, Pfister SM, Jones DTW, Fouladi M, von Bueren AO, Baudis M, Resnick A, Jones C. (2017). Integrated Molecular Meta-Analysis of 1,000 Pediatric High-Grade and Diffuse Intrinsic Pontine Glioma. *Cancer Cell* **32:**520-537.e5. doi: 10.1016/j.ccell.2017.08.017. PubMed PMID: 28966033.

Meel MH, Sewing ACP, Waranecki P, Metselaar DS, Wedekind LE, Koster J, van Vuurden DG, Kaspers GJL, Hulleman E. (2017). Culture methods of diffuse intrinsic pontine glioma cells determine response to targeted therapies. *Exp Cell Res* **360:**397-403. doi: 10.1016/j.yexcr.2017.09.032. PubMed PMID: 28947132.

Meel MH, de Gooijer MC, Guillén Navarro M, Waranecki P, Breur M, Buil LCM, Wedekind LE, Twisk JWR, Koster J, Hashizume R, Raabe EH, Montero Carcaboso A, Bugiani M, van Tellingen O, van Vuurden DG, Kaspers GJL, Hulleman E. (2018). MELK Inhibition in Diffuse Intrinsic Pontine Glioma. *Clin Cancer Res* **24:**5645-5657. doi: 10.1158/1078-0432.CCR-18-0924. PubMed PMID: 30061363.

Meers MP, Tenenbaum D, Henikoff S. (2019). Peak calling by Sparse Enrichment Analysis for CUT&RUN chromatin profiling. *Epigenetics Chromatin* **12:**42. doi: 10.1186/s13072-019-0287-4. PubMed PMID: 31300027.

Mohammad F, Helin K. (2017). Oncohistones: drivers of pediatric cancers. *Genes Dev* **31:**2313-2324. doi: 10.1101/gad.309013.117. PubMed PMID: 29352018.

Nacev BA, Feng L, Bagert JD, Lemiesz AE, Gao J, Soshnev AA, Kundra R, Schultz N, Muir TW, Allis CD. (2019). The expanding landscape of 'oncohistone' mutations in human cancers. *Nature* **567:**473-478. doi: 10.1038/s41586-019-1038-1. PubMed PMID: 30894748.

Nagaraja S, Quezada MA, Gillespie SM, Arzt M, Lennon JJ, Woo PJ, Hovestadt V, Kambhampati M, Filbin MG, Suva ML, Nazarian J, Monje M. (2019). Histone Variant and Cell Context Determine H3K27M Reprogramming of the Enhancer Landscape and Oncogenic State. *Mol Cell* **76:**965-980. doi: 10.1016/j.molcel.2019.08.030 3. PubMed PMID: 31588023.

Neph S, Kuehn MS, Reynolds AP, Haugen E, Thurman RE, Johnson AK, Rynes E, Maurano MT, Vierstra J, Thomas S, Sandstrom R, Humbert R, Stamatoyannopoulos JA. (2012). BEDOPS: high-performance genomic feature operations. *Bioinformatics* **28:**1919-20. doi: 10.1093/bioinformatics/bts277. PubMed PMID: 22576172.

Ollmann M, Young LM, Di Como CJ, Karim F, Belvin M, Robertson S, Whittaker K, Demsky M, Fisher WW, Buchman A, Duyk G, Friedman L, Prives C, Kopczynski C. (2000). Drosophila p53 is a structural and functional homolog of the tumor suppressor p53. *Cell* **101:**91-101. PubMed PMID: 10778859.

Piunti A, Hashizume R, Morgan MA, Bartom ET, Horbinski CM, Marshall SA, Rendleman EJ, Ma Q, Takahashi YH, Woodfin AR, Misharin AV, Abshiru NA, Lulla RR, Saratsis AM, Kelleher NL, James CD, Shilatifard A. (2017). Therapeutic targeting of polycomb and BET bromodomain proteins in diffuse intrinsic pontine gliomas. *Nat Med* **23:**493-500. doi: 10.1038/nm.4296. PubMed PMID: 28263307.

Quinlan AR, Hall IM. (2010). BEDTools: a flexible suite of utilities for comparing genomic features. *Bioinformatics* **26:**841-2. doi: 10.1093/bioinformatics/btq033. PubMed PMID: 20110278.

Ramírez F, Dündar F, Diehl S, Grüning BA, Manke T. (2014). deepTools: a flexible platform for exploring deep-sequencing data. *Nucleic Acids Res* **42:**W187-91. doi: 10.1093/nar/gku365. PubMed PMID: 24799436.

Ray-Gallet D, Woolfe A, Vassias I, Pellentz C, Lacoste N, Puri A, Schultz DC, Pchelintsev NA, Adams PD, Jansen LE, Almouzni G. (2011). Dynamics of histone H3 deposition in vivo reveal a nucleosome gap-filling mechanism for H3.3 to maintain chromatin integrity. *Mol Cell* **44:**928-41. doi: 10.1016/j.molcel.2011.12.006. PubMed PMID: 22195966.

Schwartzentruber J, Korshunov A, Liu XY, Jones DT, Pfaff E, Jacob K, Sturm D, Fontebasso AM, Quang DA, Tönjes M, Hovestadt V, Albrecht S, Kool M, Nantel A, Konermann C, Lindroth A, Jäger N, Rausch T, Ryzhova M, Korbel JO, Hielscher T, Hauser P, Garami M, Klekner A, Bognar L, Ebinger M, Schuhmann MU, Scheurlen W, Pekrun A, Frühwald MC, Roggendorf W, Kramm C, Dürken M, Atkinson J, Lepage P, Montpetit A, Zakrzewska M, Zakrzewski K, Liberski PP, Dong Z, Siegel P, Kulozik AE, Zapatka M, Guha A, Malkin D, Felsberg J, Reifenberger G, von Deimling A, Ichimura K, Collins VP, Witt H, Milde T, Witt O, Zhang C, Castelo-Branco P, Lichter P, Faury D, Tabori U, Plass C, Majewski J, Pfister SM, Jabado N. (2012). Driver mutations in histone H3.3 and chromatin remodelling genes in paediatric glioblastoma. *Nature* **482:**226-31. doi: 10.1038/nature10833. PubMed PMID: 22286061.

Skene PJ, Henikoff S. (2017). An efficient targeted nuclease strategy for high-resolution mapping of DNA binding sites. *Elife* **6.** *pii:* e21856. doi: 10.7554/eLife.21856. PubMed PMID: 28079019.

Skene PJ, Henikoff JG, Henikoff S. (2018). Targeted in situ genome-wide profiling with high efficiency for low cell numbers. *Nat Protoc* **13:**1006-1019. doi: 10.1038/nprot.2018.015. PubMed PMID: 29651053.

Stafford JM, Lee CH, Voigt P, Descostes N, Saldaña-Meyer R, Yu JR, Leroy G, Oksuz O, Chapman JR, Suarez F, Modrek AS, Bayin NS, Placantonakis DG, Karajannis MA, Snuderl M, Ueberheide B, Reinberg D. (2018). Multiple modes of PRC2 inhibition elicit global chromatin alterations in H3K27M pediatric glioma. *Sci Adv* **4:**eaau5935. doi: 10.1126/sciadv.aau5935. PubMed PMID: 30402543.

Tagami H, Ray-Gallet D, Almouzni G, Nakatani Y. (2004). Histone H3.1 and H3.3 complexes mediate nucleosome assembly pathways dependent or independent of DNA synthesis. *Cell* **116:**51-61. PubMed PMID: 14718166.

Toledo CM, Ding Y, Hoellerbauer P, Davis RJ, Basom R, Girard EJ, Lee E, Corrin P, Hart T, Bolouri H, Davison J, Zhang Q, Hardcastle J, Aronow BJ, Plaisier CL, Baliga NS, Moffat J, Lin Q, Li XN, Nam DH, Lee J, Pollard SM, Zhu J, Delrow JJ, Clurman BE, Olson JM, Paddison PJ. (2015). Genome-wide CRISPR-Cas9 Screens Reveal Loss of Redundancy between PKMYT1 and WEE1 in Glioblastoma Stem-like Cells. *Cell Rep* **13:**2425-2439. doi: 10.1016/j.celrep.2015.11.021. PubMed PMID: 26673326.

Venneti S, Santi M, Felicella MM, Yarilin D, Phillips JJ, Sullivan LM, Martinez D, Perry A, Lewis PW, Thompson CB, Judkins AR. (2014). A sensitive and specific histopathologic prognostic marker for H3F3A K27M mutant pediatric glioblastomas. *Acta Neuropathol* **128:**743-53. doi: 10.1007/s00401-014-1338-3. PubMed PMID: 25200322.

Wang X, Long Y, Paucek RD, Gooding AR, Lee T, Burdorf RM, Cech TR. (2019). Regulation of histone methylation by automethylation of PRC2. *Genes Dev* **33:**1416-1427. doi: 10.1101/gad.328849.119. PubMed PMID: 31488576.

Wu G, Broniscer A, McEachron TA, Lu C, Paugh BS, Becksfort J, Qu C, Ding L, Huether R, Parker M, Zhang J, Gajjar A, Dyer MA, Mullighan CG, Gilbertson RJ, Mardis ER, Wilson RK, Downing JR, Ellison DW, Zhang J, Baker SJ, *et al*. (2012). Somatic histone H3 alterations in pediatric diffuse intrinsic pontine gliomas and non-brainstem glioblastomas. *Nat Genet* **44:**251-3. doi: 10.1038/ng.1102. PubMed PMID: 22286216.

Acknowledgements
We thank Ekaterina Babaeva, Shelli Morris and Matthew Biery for technical assistance. We thank Michelle Monje (Standford University) for providing SU-DIPG-IV, SU-DIPG-XIII, SU-DIPG-XVII and SU-DIPV-XXXVI cell lines, Esther Hulleman VU University Medical Center, Amsterdam) for providing the VUMC-DIPG-10 line, Eliza Small for MTF2 antibody, Christine Codomo for library preparation, and Srinivas Ramachandran for helpful discussion and analysis. J.F.S is supported by a Damon Runyon-Sohn Foundation Fellowship, received support from NIH NCI Training Grant T32 CA009351 and an Alex's Lemonade Stand Young Investigator Award. This work was funded by the HHMI (S.H.) and by the NIH (R01GM108699, K.A.).

Competing interests: All authors declare no competing interests.

Data accessibility:
GEO accession GSE118099.

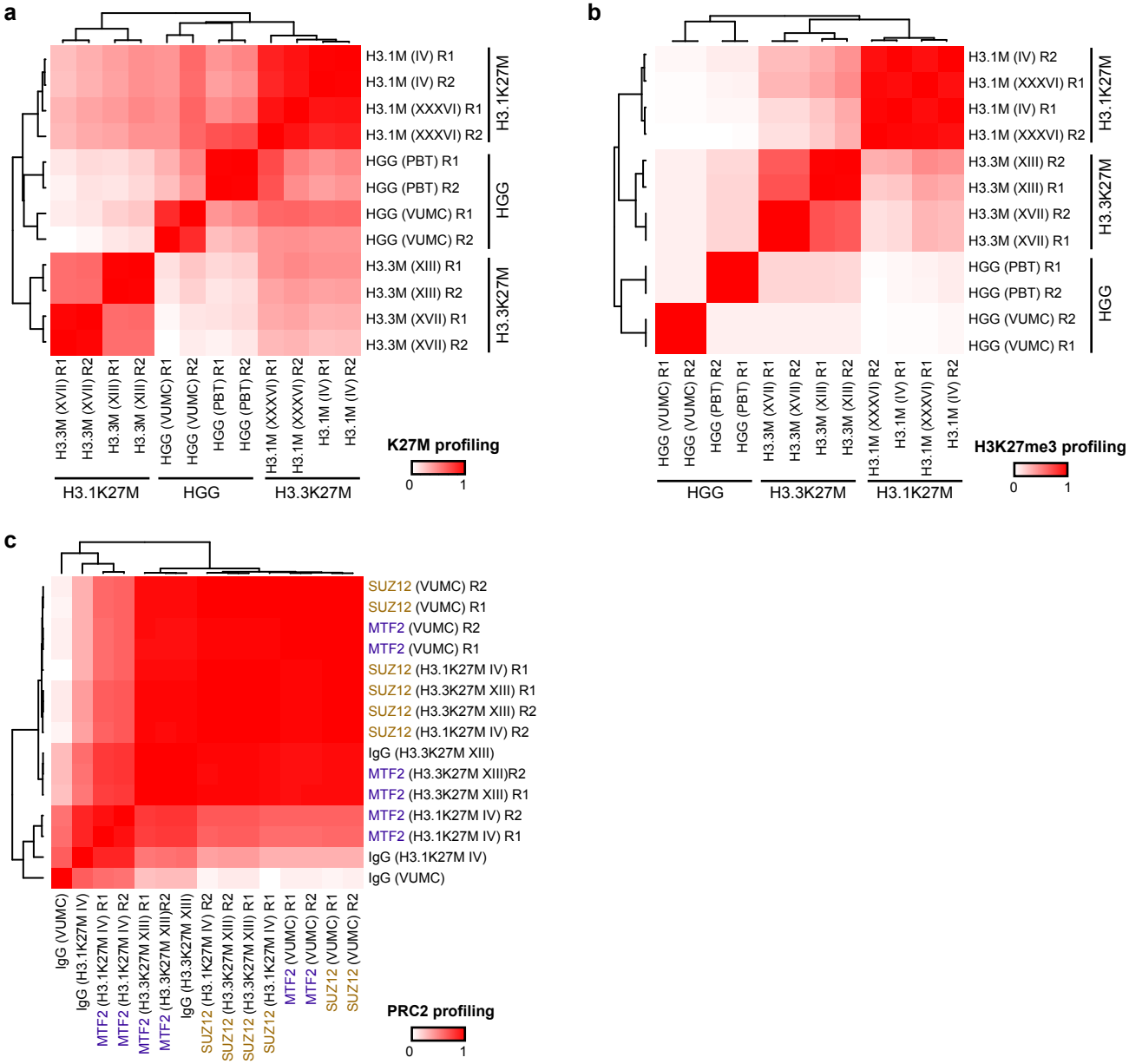

Figure 3 – figure supplement 1. Reproducibility of chromatin profiling experiments. Heatmaps display Pearson's correlation (R^2) between denoted cell line replicates (R1 or R2) for CUT&RUN signal from H3K27M (A), H3K27me3 (B), or PRC2 subunits SUZ12 and MTF2 (C).

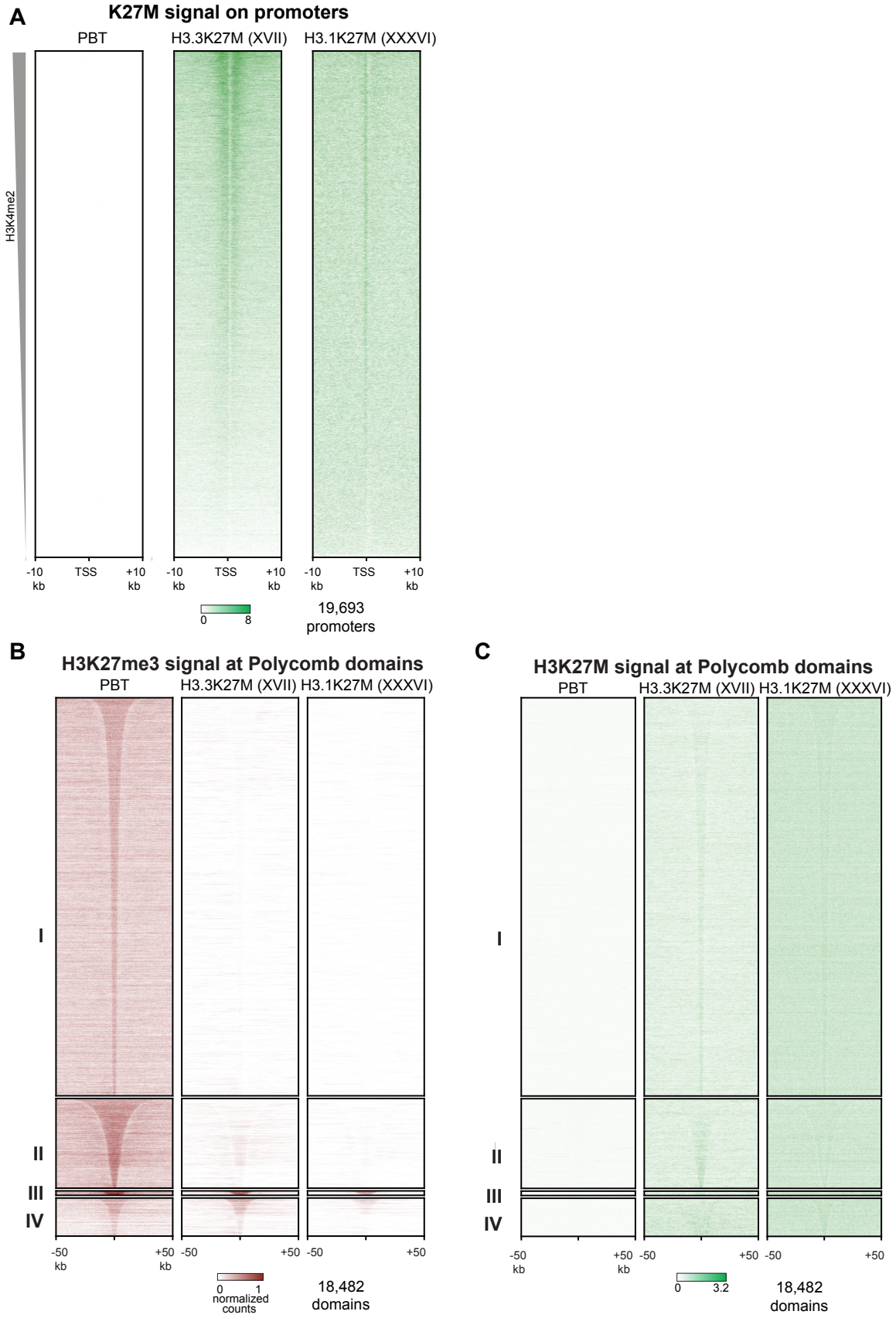

Figure 3 – figure supplement 2. Analyses of PBT-04 HGG and DIPGXVII and DIPGXXXVI glioma cell lines. (A) Heat maps of H3K27M CUT&RUN signal on gene promoters in HGG and glioma cell lines, ordered by H3K4me2 CUT&RUN signal as in Figure 3D. (B) Enrichment of H3K27me3 in HGG and glioma cell lines in differential H3K27me3 clusters defined in Figure 4A.

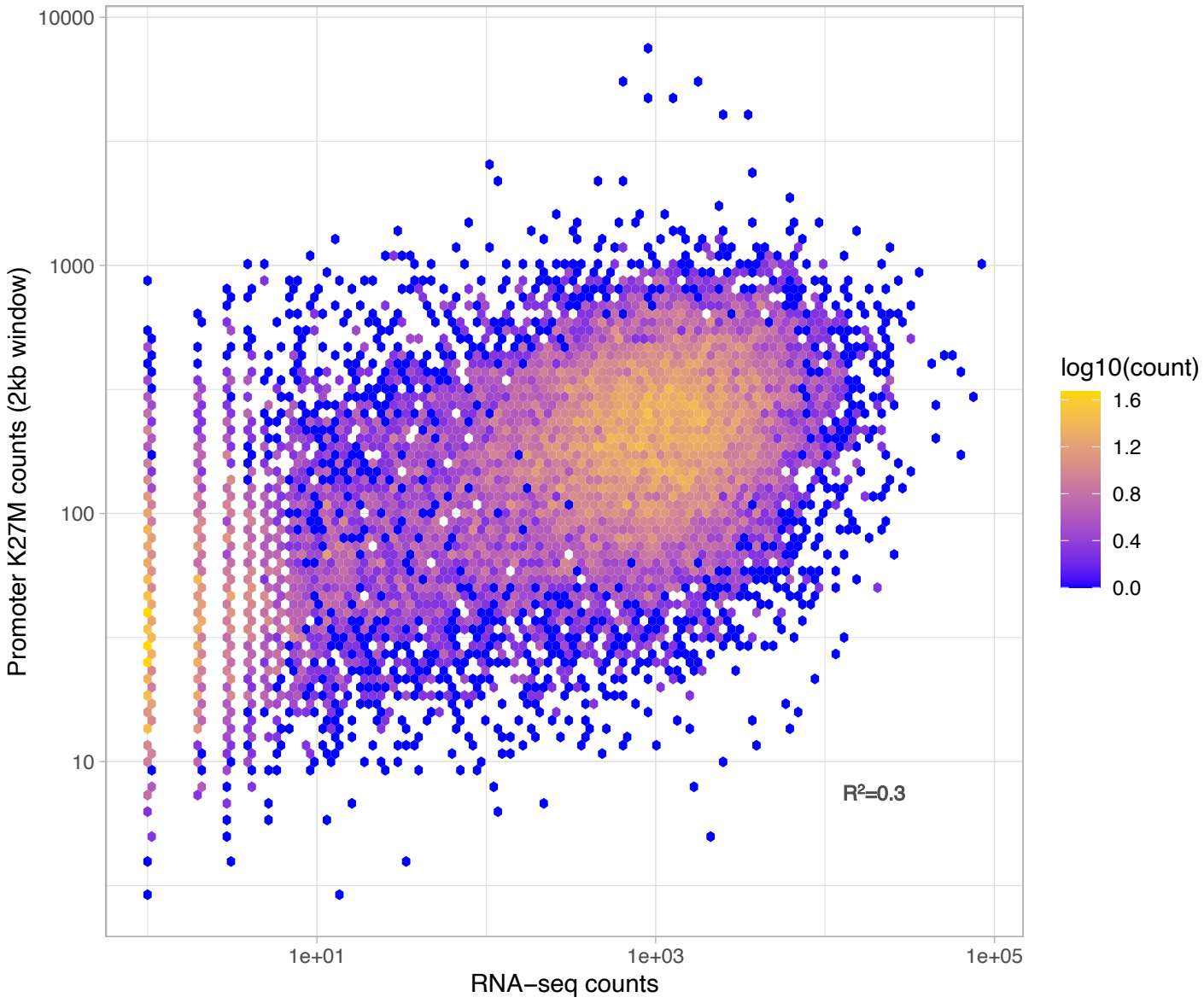

Figure 3 – figure supplement 3. Overlap between RNA-seq signal and H3K27M-enriched regions in the SU-DIPG-XIII cell line.

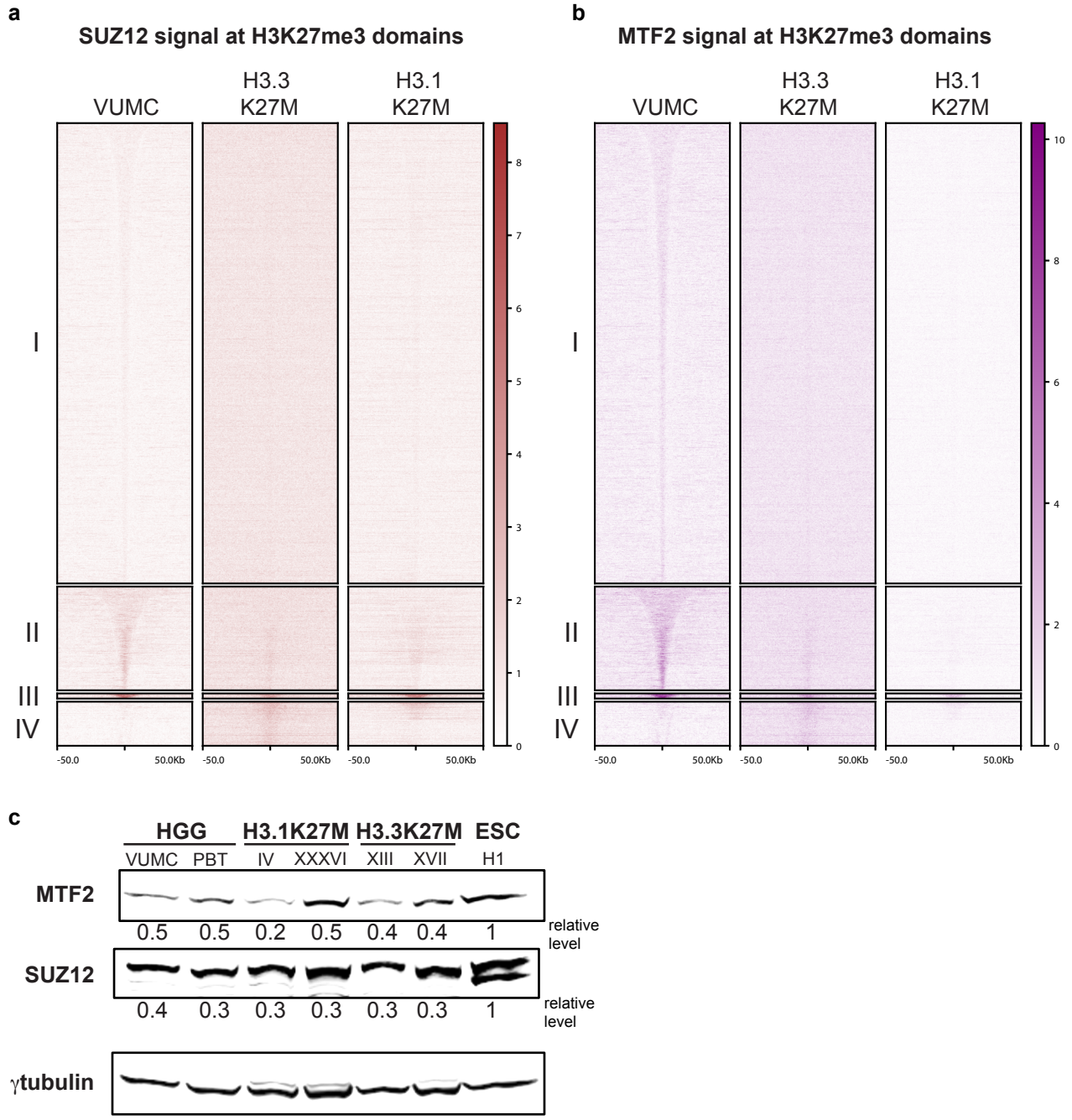

Figure 5 – figure supplement 1. Enrichment of PRC2 in H3K27me3 domains. CUT&RUN signal for SUZ12 (brown, left) or MTF2 (purple, right) in differential H3K27me3 domains defined in Figure 4A.

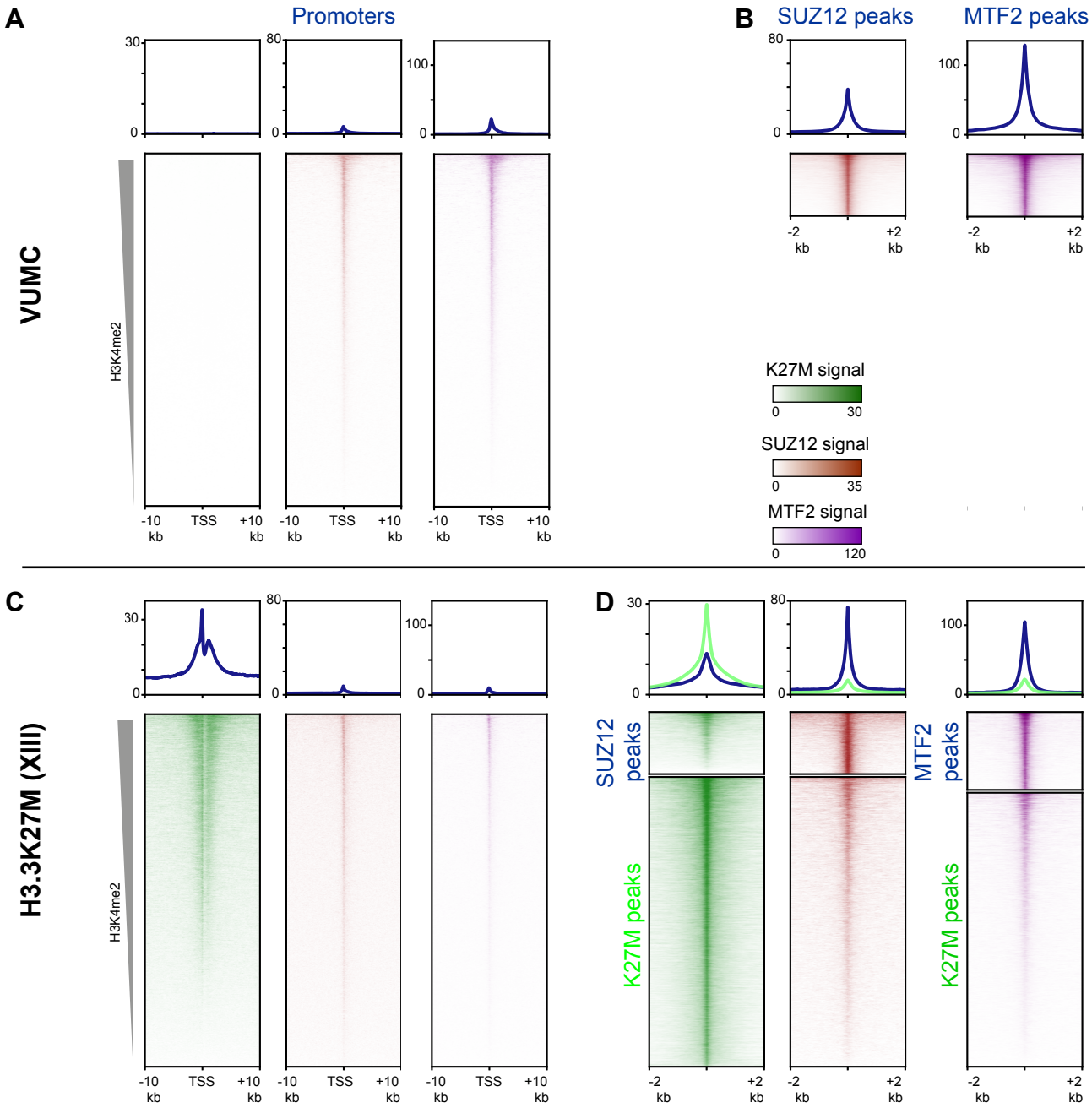

Figure 5 – figure supplement 2. Enrichment of PRC2 components at sites of active histone turnover. Enrichment of K27M (green), SUZ12 (brown), or MTF2 (purple) CUT&RUN signal at indicated regions, scaled by CUT&RUN target. (A) and (C): Enrichment at promoters ordered by H3K4me2 signal in VUMC (A) or XIII (C). (B) and (D): Enrichment at PRC2 and K27M peaks in VUMC (B) and XIII (D).

Supplementary File 1. MSExcel spreadsheets of all called peaks and domains from profiling experiments.

Supplementary File 2. Gene IDs for H3K27M-enriched peaks from H3K27M CUT&RUN performed in H3.3K27M-mutant DMG cell lines.

Supplementary File 3. Sequencing read counts for each CUT&RUN profiling experiment.

Supplementary File 4. Gene Ontology term analysis for genes overlapped by differential H3K27me3 domains in Cluster IV.

Supplementary File 5. Oncoplex sequencing results of the H3K27M-positive high grade glioma cell lines.